Interdiffusion and reaction of metals: The influence and relaxation of mismatch-induced stress

F. Hartung and G. Schmitz*
Institut für Materialphysik, Universiät Göttingen, Hospitalstr. 3-7, 37073 Göttingen, Germany
(Received 22 March 2001; published 6 December 2001)

The early interdiffusion stages in epitaxially grown Ag/Au and Cu/Au reaction couples are investigated by high-resolution and *Z*-contrast electron microscopy. While the interdiffusion in the lattice-matched system Ag/Au follows Fick's diffusion laws from the very beginning, a complex two-stage reaction is observed in the lattice-mismatched Cu/Au samples. A fast diffusion at the beginning of the heat treatment produces a planar zone of lattice defects along the interface, which release most of the induced stress. This first reaction stage stops after reaching a diffusion length of about 15 nm. Subsequent interdiffusion takes place by a recrystallization mechanism comprising heterogeneous nucleation of new grains and diffusion-induced grain boundary migration. During this second reaction stage, discontinuous composition profiles are determined, evidencing stress release at high-angle grain boundaries. The recrystallization mechanism also dominates the formation of ordered intermetallics at lower reaction temperatures.

DOI: 10.1103/PhysRevB.64.245418 PACS number(s): 66.30.Ny, 66.30.Pa, 68.37.Lp, 68.55.Ac

I. INTRODUCTION

Motivated by important applications in data storage and magnetic sensoric, stability and potential reactions of metallic multilayers are a long-term interest of material physics. With continuous downscaling of the devices, the earliest diffusion stages deserve particular attention. Very steep composition gradients establish a situation far from equilibrium, so that phenomena beyond the near-to-equilibrium physics of Fick's laws may develop. In early work, this question was addressed by the introduction of nonlinear diffusion equations[1,2] taking into account gradient energy and contributions of elastic strain to the free energy. More recently, Larché and Cahn[3,4] discussed the influence of reaction-induced stress in more detail, and Stephenson[5] includes plastic relaxation in continuum models, which were successfully applied to the interdiffusion of amorphous Ni/Zr layers.[6]

The mentioned studies assume that a planar geometry is preserved during all interdiffusion stages and, furthermore, vacancy equilibrium is maintained. Our experimental study demonstrates that this assumption may not be justified in the case of crystalline materials because of the coherency constraint and microstructure of the metallic films. We investigate the interdiffusion of two fcc metals Cu and Au at temperatures that exclude the formation of any intermetallic compound. At first, this seems to be a very simple situation, but the reaction turns out to be complex, since these two metals are distinguished by a substantial lattice mismatch. The microscopic mechanisms of stress relaxation and atomic transport are determined by high-resolution electron microscopy (HREM) and *Z*-contrast electron microscopy of cross sectional specimens. In order to identify the reasons for the observed microstructural transformation and to test the reliability of the applied analysis methods, the results are directly compared to those obtained at Ag/Au, where no deviations from Fick's laws are expected as the mismatch is negligible and the mobilities of both species Ag and Au are very similar.[7]

II. EXPERIMENT

Ag/Au and Cu/Au reaction samples were produced by ion beam sputtering. After suitable heat treatments, cross sectional specimens of the reaction zone were prepared and investigated by transmission electron microscopy (TEM). Conventional bright-field and high-resolution phase contrast imaging were performed to obtain direct information on the microstructural development. To achieve also spatially resolved chemical information, dark-field images were taken under high-angle hollow-cone dark-field (HCDF) illumination. In addition, macroscopic measurements by x-ray diffractometry (XRD), secondary neutral particle spectrometry (SNMS), and differential scanning calorimetry (DSC) were performed. Since these methods average over a larger specimen volume, they complement the microscopic measurements by an improved statistics.

A. Specimen preparation

To facilitate correct orienting of the specimens for HREM, single-crystalline substrates of Cu or Ag were used for thin-film deposition. Furthermore, single-crystalline substrates favor a coarse-grained microstructure of the metallic films with two preferred orientation relations across the interfaces. The substrates were cut by spark erosion, mechanically ground, and electrolytically or chemically polished to remove any mechanical damage. In addition, they were cleaned inside the deposition chamber using a 600 eV Ar beam immediately before coating. The background pressure of the chamber was better than 10^{-6} mbar. Metallic thin films were deposited on water-cooled substrates with a deposition rate of 10–20 nm/min. Switching between cleaning and deposition and between different targets was done within a second to avoid any contamination. With SNMS, no impurities were detected at the interfaces, although the method can detect material in the ppm range.

For TEM and SNMS, layer structures were produced comprising two to five single layers, each 60–150 nm in thickness. Further samples were deposited on glass substrates to eliminate the strong x-ray signal of the metallic substrates. For DSC measurements, multilayers with 25 and 50 nm single-layer thickness were deposited on glass substrates coated by a sodium metaphosphate film,[8] which could be solved in water to obtain unsupported multilayer samples.

TABLE I. Model parameter to describe the high-angle scattering cross section.

Cu			Ag			Au		
λ/[nm]	b	γ	λ/[nm]	b	γ	λ/[nm]	b	γ
6.0	58	0.87	5.5	40	0.90	4.8	25	0.91

To protect the thin films during cross sectional preparation, a further Cu substrate was glued onto the deposited films and subsequently these packages cut to small disks of 0.5 mm thickness. Heat treatments at the microscopy specimens were performed in this intermediate preparation stage. Using a salt bath furnace, annealing times of a few seconds could be realized. The disks were ground to 0.10 mm during the further preparation steps so that regions of direct contact to the salt bath were reliably removed. Thinning of the specimens to electron transparency followed established procedures[9] by dimple grinding and ion milling.

Thin-film specimens for the SNMS analysis and XRD were always covered by a final Au layer. In addition they were wrapped into a thin Au foil before immersing into the heated salt bath to prevent surface reactions.

B. Chemical imaging by hollow-cone illumination

In most cases, the interpretation of electron micrographs in terms of local composition is not possible, since dynamical diffraction effects mask the desired mass contrast. However, the disturbing coherent contrast phenomena are significantly suppressed, if a hollow cone illumination[10] is used to produce high-angle HCDF images. We demonstrated in previous work[11] that under suitable illumination conditions the image contrast of this *Z*-contrast method is well approximated by an incoherent multiscattering model, so that a local chemical analysis becomes possible by an evaluation of image intensities. Provided sufficient specimen quality, the spatial resolution of the method ranges down to about 1 nm and the chemical accuracy to a few at. % if calibration points of known composition are used in the analyzed area.

For the chemical analysis in this work, we followed the experimental procedure described previously.[11] The necessary scattering parameters λ, b, and γ defined in that publication are adapted to intensity data of pure Cu, Ag, and Au. Numerical data are given in Table I. Compared to our previous work,[11] values for Cu and Au are redetermined to improve the description over an extended range of scattering angles.

As the quantitative evaluation of HCDF images is not well established yet, we studied at first the interdiffusion of Ag/Au films, for which we did not expect deviations from Fick's laws, to confirm the feasibility of the analysis and then addressed the more complex case of Cu/Au.

III. CHARACTERIZATION OF THE AS-DEPOSITED STATE

In the case of Ag/Au the lattice mismatch $\eta=(a_{Ag}-a_{Au})/a_{Au}$ amounts to only 0.2%, which favors a coherent interface between both metals. In Fig. 1, a cross section of a specimen in the as-prepared state is shown. The lateral size of the grains exceeds 150 nm. Inside the layers, twins are found in high number density, which is explained by the low stacking fault energy of 20 mJ/m^2 and 40 mJ/m^2 in Ag and Au, respectively.[12] From the parallel alignment of the coherent twin boundaries in different layers epitaxial growth, favoring a direct transition between both lattices, is quite obvious. Epitaxial growth was further proved by texture measurements showing a very sharp texture of the deposited layers in agreement with the orientation of the substrate.[13]

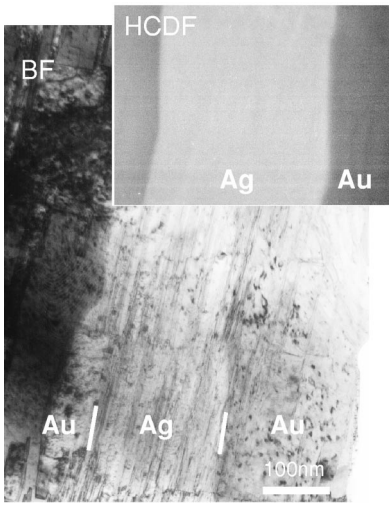

FIG. 1. Cross-sectional image of an Ag/Au multilayer. Five single layers, each 150 nm in thickness, were deposited on a Ag substrate. The parallel line contrasts originate from lattice twins. In addition, irradiation defects caused by ion milling are visible as black dots. The HCDF image reproduced in the inset was recorded at a thick specimen area ($t>20$ nm), where Ag appears brighter than Au. The contrasts of lattice twins and irradiation defects are remarkably suppressed.

In the case of Cu/Au, we face a very different situation. With about 12%, the lattice mismatch is so pronounced that epitaxial growth seems not to be very likely. Nevertheless, we do observe a strong texture in the deposited layers, corresponding to the orientation of the Cu substrates. Epitaxial growth in this layer system was also reported previously.[14] By microscopy, we observe a coarse-grained microstructure similar to that of the Ag/Au specimens. Using HREM, two dominating interface types are identified as presented in Fig. 2. A direct transition with almost no misorientation between both fcc lattices (a) and the twin relation (b). To release the coherency stress misfit dislocations are introduced if the layer thickness exceeds a certain critical one. As the elastic energy of a homogeneously strained volume scales with the square of the misfit while that of the misfit dislocation network scales only linearly, this critical thickness decreases with increasing lattice mismatch. For a mismatch of 9%, it ranges already down to about one lattice constant.[15] Thus, regarding the thickness of the layers under consideration, the density of misfit dislocations should correspond to the natural lattice mismatch; i.e., their theoretical spacing amounts to only 2 nm, so that individual dislocation cores are hardly

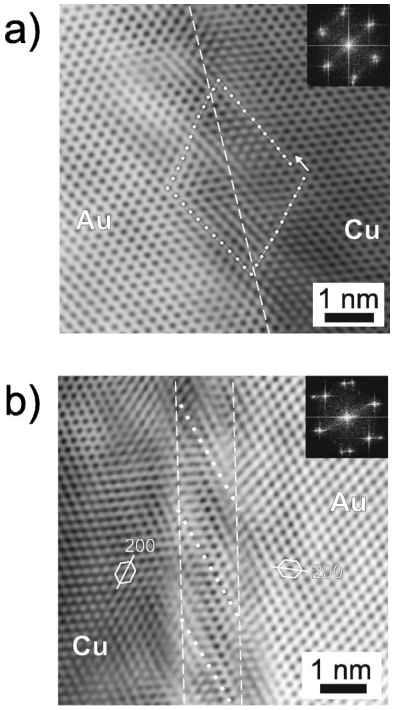

FIG. 2. HREM of the interface between Cu and Au layer, (a) direct lattice transition $\Sigma=1$, (b) twin relation $\Sigma=3$.

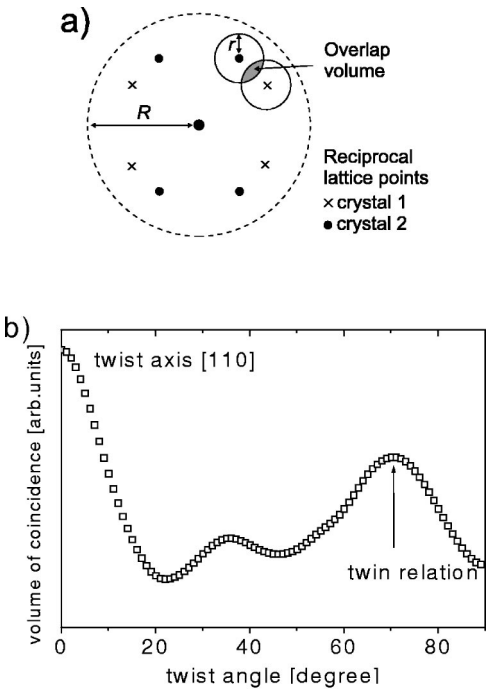

FIG. 3. Lattice coincidence in reciprocal space: (a) definition of the overlap criterion, (b) degree of lattice coincidence between Cu and Au lattices twisted around a [011] axis ($r=0.2/a_{\mathrm{Au}}, R=4/a_{\mathrm{Au}}$).

identified. For example, the Burgers circuit sketched in micrograph (a) indicates already two additional {111} layers on the Cu side terminated by complete lattice dislocations with Burgers vectors $a/2(011)$, but the exact localization of the dislocations inside the circuit remains difficult. Beside these dislocations, we usually observe in the case (a) a slight misorientation. Both lattices are rotated to each other by $2°-3°$ around a $\langle 011\rangle$ axis.

In the twin case (b), the structural interface appears to be broadened to a width of 1 nm. In the micrographs, this width remained constant, when specimen areas of different foil thickness were imaged. Thus, an artifact caused by a misalignement of the interface can be ruled out. Two layers of increased defect density, marked in Fig. 2(b) by a pair of dashed lines, appear with a blurred fringe contrast. They are separated by a zone of more perfect lattice order. Although no individual dislocations can be localized in the micrograph, this observation allows the conclusion that part of the misfit dislocations glide or climb out of the geometric interface plane. When an extended region of the interface is evaluated, a periodic variation of the fringe contrast along the interface becomes obvious, indicated by dotted lines in the figure. The oscillation length amounts to 2 nm, in good agreement with the theoretical dislocation spacing. This periodicity allows to consider the observed interphase boundaries similar to high-angle grain boundaries in homogeneous materials, which consist usually of building units repeated periodically along the interface. If the coincidence site lattice (CSL) classification of homophase grain boundaries is generalized to heterophase boundaries, the observed interface types may be classified as $\Sigma=1$ and $\Sigma=3$.

The geometric definition of the CSL is only useful if the two lattice parameters exactly match the ratio of two small integers. To overcome this difficulty, Pirouz and co-workers suggested to measure the agreement between two different crystals by the amount of overlap in the reciprocal space.[16] A sphere of radius r is defined around each reciprocal lattice point and the overlapping volumes between the spheres of both lattices are added within a restricted region of the reciprocal space defined by the radius R [see Fig. 3(a)]. This way, each interface is assigned a certain degree of overlap—in other words, a certain degree of atomic matching. We calculated the overlap for different orientation relations between Cu and Au, and indeed it is found that $\Sigma=1$ and $\Sigma=3$ boundaries are distinguished by the best lattice matching as demonstrated in Fig. 3(b) for a twist around the [011] axis.

Beside the structural characterization of the prepared interfaces, also their chemical properties are of interest. The aforementioned hollow-cone illumination enables a spatially resolved analysis such that both interface types can be characterized independently. Figure 4 shows composition profiles determined normal to the interfaces. The broader structural width of the twin boundary is reflected by a slightly increased intermixing. However, the difference is only minor. Roughly, the depth of initial solution amounts to 2 nm in both cases, which is slightly larger than found by Gladyszewski[17] in Cu/Au layer systems or typically found by atomprobe tomography in similar metallic reaction couples.[18–20] Regarding the resolution limit of HCDF imaging, about 1 nm, and potential misorientation or roughness of the interface, this discrepancy may not be significant.

To understand the interdiffusion reactions presented later,

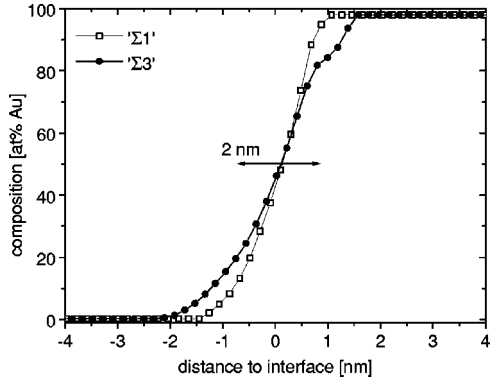

FIG. 4. Composition profiles determined by HCDF imaging at as-prepared Cu/Au interfaces. To reduce local fluctuations, for each interface type data obtained at six different positions were averaged.

it is important to realize that the overwhelming fraction of the interphase boundary in our specimens consists of only two interface types. In both cases, the adjacent lattices have at least one set of densely packed {111} planes in common. In the case of Cu/Au, about every eighth of these planes is terminated by a dislocation close to the interface to accommodate the difference in the lattice parameters.

IV. MACROSCOPIC ANALYSIS OF INTERDIFFUSION

To obtain an overview on the specimen behavior and to determine suitable temperatures, the interdiffusion of both reaction couples was investigated by neutral secondary particle spectrometry. Compared to ordinary secondary-ion mass spectrometry, the sputtered secondary particles are additionally ionized by a laser beam. In this way, a reliable analysis gets possible even for species, for which the ionization probability during sputtering is rather low.

Isothermal heat treatments were interrupted several times to perform a depth profiling. As an example, Fig. 5 shows composition profiles, which were obtained during the annealing of a $Au_{60\ nm}/Cu_{60\ nm}/Au_{60\ nm}$ triple layer deposited on a Cu single crystal. These measurements are presented and discussed in detail elsewhere.[13] In the present context it is sufficient to study the depth profiles in a very simple manner, working out a remarkable difference between the Ag/Au and

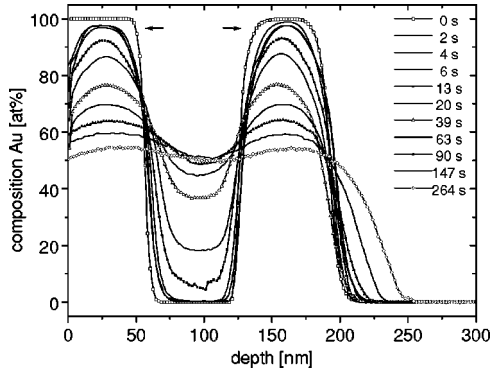

FIG. 5. Compositional depth profiles of a Au/Cu/Au/Cu specimen obtained by SNMS during annealing at 430°C. Arrows point at the reaction break between 2 and 10 s annealing time.

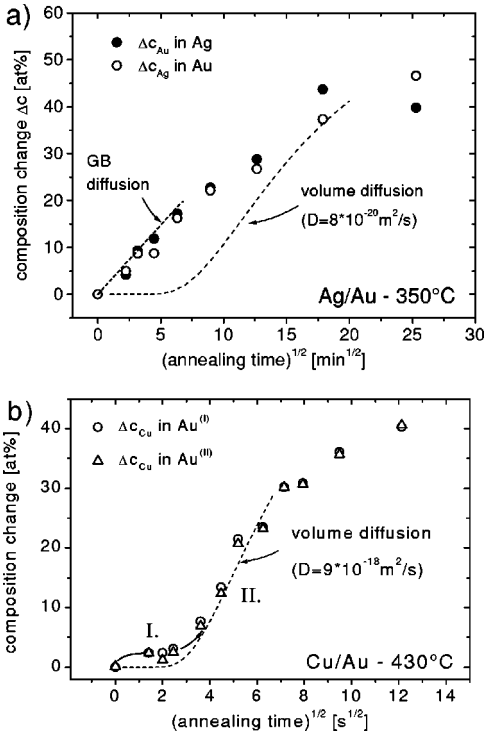

FIG. 6. Variation of peak compositions in the center of the layers. (a) Ag/Au at 350°C, single-layer thickness 100 nm and (b) Cu/Au at 430°C, single-layer thickness 60 nm.

Cu/Au samples. For that, we plot the change of the peak compositions determined at the middle of the various layers versus the annealing time as presented in Fig. 6. Since it is probably influenced by the free surface, we disregard the Au top layer. Dashed lines indicate the behavior expected for volume diffusion according to Fick's laws.

In the case of Ag/Au annealed at 350°C [Fig. 6(a)], the peak compositions change monotonously. At later stages, the kinetics corresponds to ordinary volume diffusion. The fast mixing in the early stages is explained by grain boundary diffusion (dashed line).[13] Using the local chemical analysis provided by HCDF imaging, the boundary effect can be separated by determining composition profiles far from any grain boundary. Profiles of this kind, determined normal to the layer interface, are shown in Fig. 7. From the very beginning, they agree with the solution

$$c(x,t)=\frac{c_0}{2}\,\mathrm{erfc}\left(\frac{x}{2\sqrt{Dt}}\right) \tag{1}$$

of the diffusion equation, as indicated in the figure by solid lines. If the initial mixing of the as-deposited state is taken into account by a suitable time shift, a diffusion coefficient of $8\times10^{-20}\mathrm{m}^2/\mathrm{s}$ is determined at 350°C, which agrees very well with an extrapolation of the available literature data for the interdiffusion coefficient.[21,22,23,24] We do not observe any hints at further effects, such as the formation of ordered interface phases described in previous work.[25] The agreement of the result with literature data demonstrates the reliability

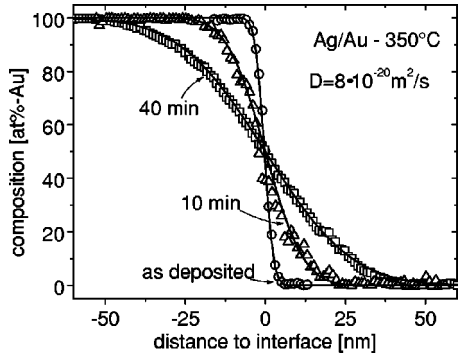

FIG. 7. Microscopic composition profiles determined by HCDF imaging at the interface between Ag/Au. To reduce the influence of local fluctuations, the profiles shown here are averaged over six individual measurements.

of our chemical analysis method; thus we also expect reliable results in the case of Cu/Au, where the scattering contrast is even more pronounced.

The data of similar experiments with Cu/Au demonstrate a very different behavior; see Fig. 6(b). Again, a fast interdiffusion (I) takes place at the beginning, which leads to the solution of 2–3 at. % Cu inside the Au layers. However, this first reaction stops already after 2 s of annealing. A further development (II) is only noticed after a resting period of about 12 s. This way, the Cu/Au data indicate a two-step reaction mechanism.

Another remarkable behavior of the Cu/Au system is observed by x-ray diffractometry. As both components possess a very different lattice parameter, the composition of the binary alloy may be deduced from the diffraction angle of a given set of lattice planes. In Fig. 8, x-ray spectra are reproduced as obtained during the annealing of a $(Au_{60\ nm}/Cu_{60\ nm})_n$ multilayer. Only the angle range containing the (111) peaks of Au and Cu is shown. As expected, the reflections of both pure components are found in the as-deposited state. We would expect these reflections to broaden because of the continuous composition profiles established by interdiffusion and finally to meet into a central new reflection, corresponding to the completely intermixed alloy. The experimental spectra, however, develop several

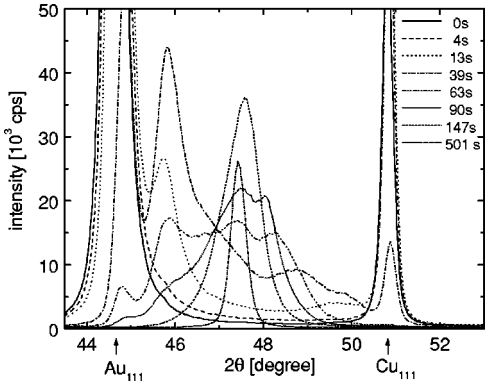

FIG. 8. X-ray spectra of a Cu/Au multilayer obtained in θ-2θ geometry during annealing at 430°C (Co $K\alpha$ radiation: $\lambda = 0.1791$ nm).

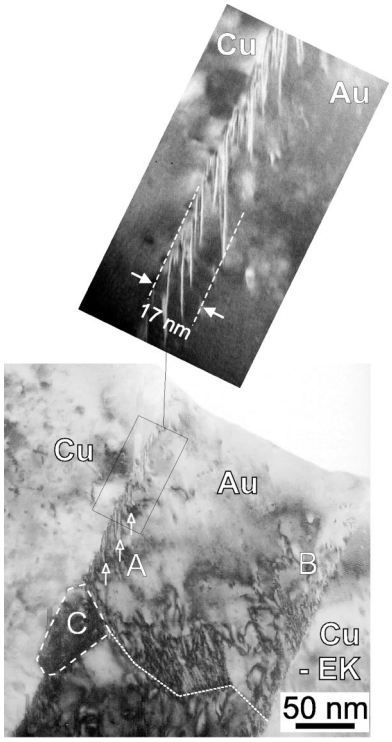

FIG. 9. BF cross section image of a Cu/Au/Cu(s.c.) specimen after 5 s annealing at 430°C. Interface types at mark (A) $\Sigma 3$, at (B) $\Sigma 1$. A nucleus of a new grain formed already at (C). The dotted line emphasizes a small angle grain boundary across the Au layer. Imaging was performed under two beam condition to optimize the contrast of structural defects.

intermediate maxima, which indicate the formation of regions of different preferred compositions inside the diffusion zone. This result is even more striking considering that the diffusion temperature was chosen significantly above the highest-order transition to prevent the formation of any ordered intermetallic phase. Indeed, the absence of ordered phases is confirmed by the absence of superlattice reflections in the XRD spectra and electron diffraction patterns.

V. MICROSCOPIC ANALYSIS OF THE INTERDIFFUSION IN CU/AU

The aforementioned experiments indicate that the interdiffusion of Cu/Au proceeds in two subsequent reaction steps. However, only microscopic investigations can prove this hypothesis and reveal the underlying mechanism on the atomic scale.

A. Mechanism of the first reaction stage

In Fig. 9, a Cu/Au reaction couple deposited onto a Cu substrate is shown after 5 s annealing at 430°C. The chosen aging time falls well into the regime of the proposed first reaction stage. If the annealed specimen is compared to an as-deposited one (BF and HCDF images of the initial stage have been published previously[26]), platelike defects, appearing as needles in the two-dimensional (2D) projection, have developed at the interface, which becomes particular clear at

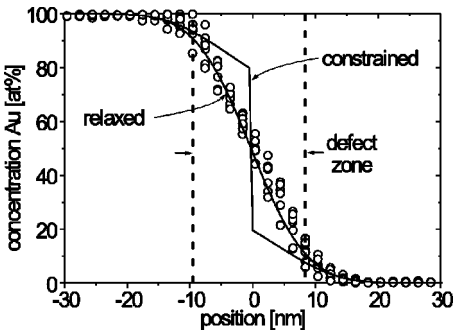

FIG. 10. Composition profile at a Cu/Au interface after annealing 430°C/5 s determined by HCDF imaging.

the twin type boundary, where the defects are oriented parallel to the common {111} plane set [see interface at (A) in the figure]. The image at the top shows a part of such a defect zone at increased magnification. The defects are found inside a band along the original interface with a homogeneous thickness of 17 nm.

By compositional analysis based on HCDF images, it is demonstrated that the formation of the observed defects is indeed related to an intermixing of both components. Data of the analysis are shown in Fig. 10. The scattering points represent measurements at different lateral positions along the interface. On the average, however, a well-defined continuous profile across the defect band is obtained. The position of the structural defects relative to the diffusion profile is indicated by dashed lines. Obviously, they are introduced when the intermixing exceeds about 10 at. % at the Au and the Cu side as well.

The atomistic structure of the observed defects is elucidated by high-resolution microscopy. Figure 11(a) shows a phase contrast image of a twin-type interface after 5 s heat treatment at 430°C. The adjacent lattices appear reflected at the common $(11\bar{1})$ plane, so that both lattices can be separated easily as shown by the white line. The needlelike defects noticed in the conventional bright-field images correspond to spikes of Cu lattice orientation growing into the Au crystal. This way, the original planar interface becomes extremely rough.

How is this lattice transformation achieved? To answer this question the fringe contrast was analyzed in detail by comparison to electron optical simulations performed with established simulation software.[27] Technical details of this procedure are described elsewhere.[13] The essential results explaining the reaction mechanism are illustrated by three enlarged details shown in the lower part of Fig. 11.

At the needle's tip, we notice an inserted densely packed plane, which ends in a Frank-type prismatic dislocation $b=[11\bar{1}]a/3$, as is demonstrated in Fig. 11(b). Because of the additional lattice plane, the stacking sequence is locally transformed into that of the related twin, which is shown in Fig. 11(c). By comparison with simulated HRTEM images of different structure models, it is proved that the additional plane is bounded by a prismatic dislocation; no further relaxation by another Shockley partial, transforming the sessile prismatic dislocation into a glissile one, is found. In the figure, part of a simulated image showing the best matching to the experimental one is inserted.

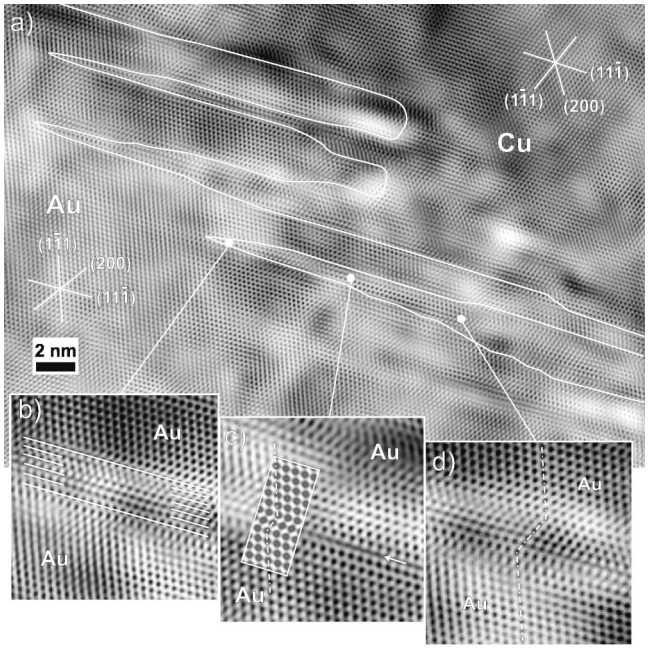

FIG. 11. (a) phase contrast image of structural defects formed at a Cu/Au interface by 5 s annealing at 430°C. The adjacent lattices are oriented in twin relation. Both lattices are imaged in (011) zone axis orientation, defocus chosen close to Scherzer focus. (b)–(d) several details observed along one needlelike structure. Locations as indicated in (a). A noise filter was applied to improve the reproduction.

Towards the Cu side, the needles grow in thickness, which means on the atomic scale that further lattice planes are ''switched'' into the stacking sequence of the Cu crystal, as shown in Fig. 11(d). This is achieved by conservative motion of Shockley partials with Burgers vectors $b_1=[112]a/6$ or $b_2=[2\bar{1}1]a/6$, which are able to glide on the common $(11\bar{1})$ plane. Also, further additional lattice planes are inserted by the described climb mechanism to accommodate the difference of the lattice constants.

In the case of a $\Sigma=1$ boundary, the introduction of additional lattice planes is observed in the same manner. Their habit plane is chosen randomly out of the existing four possibilities. However, as in this case no rotation of the lattice is required, the defects show a much weaker-contrast (see Fig. 9) interface at (B). Beside partials, which are necessary to restore the previous stacking sequence at inserted planes, now complete lattice dislocations contribute also to the relaxation of the misfit stress.

B. Mechanism of second reaction stage

Surprisingly, the described semicoherent reaction shows no development with further annealing. We observe the defect band as well as the diffusion profiles between 3 s, the shortest time which could be realized in the experiment, and 15 s with a comparable width, which leads to the conclusion that this first reaction step proceeds very fast initially, but ceases when a reaction layer thickness of 15–20 nm is

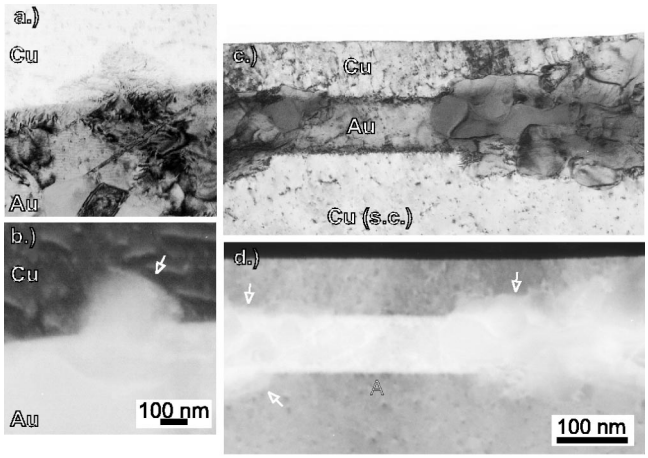

FIG. 12. BF (a), (c) and HCDF (b), (d) images of a Cu/Au reaction couple after annealing at 430°C for 5 s (a), (b) and 10 s (c), (d).

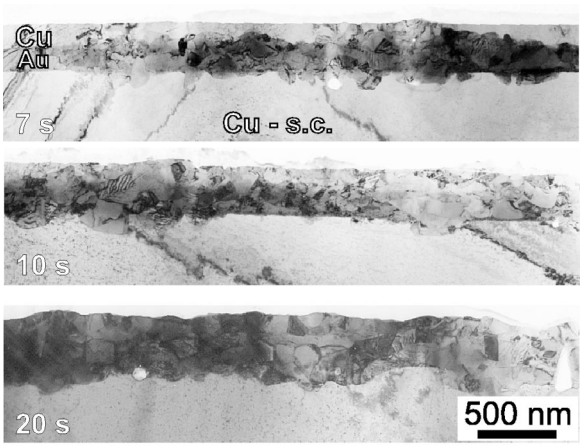

FIG. 13. Cross section images of a Cu/Au/Cu(s.c.) specimen after different annealing times.

reached. Instead, a second process dominates the interdiffusion process after about 15 s annealing. It is seen to be initialized already after 5 s annealing in the micrograph of Fig. 9. At the position marked (C), a grain of only 30–50 nm size is observed, which extends somewhat into the Cu lattice and has not developed the needlelike defect structure at its boundary. As grains of this size are not observed in the as-deposited stage, obviously a new grain has nucleated at a triple point, where previously a small-angle grain boundary met the interface.

Further stages of this process are shown in Fig. 12, where BF images (a),(c) are compared to the corresponding HCDF images (b),(d). Again, chemical transport related to the structural transformation is detected. In Figs. 12(a) and 12(b), a new grain nucleated at the interface. Without doubt, the formation of the new grain is related to a transport of Au into the Cu lattice.

Figures 12(c) and 12(d) show a specimen after 10 s annealing. At this intermediate reaction stage, the newly formed grains are organized in clusters, heterogeneously distributed along the interface as seen at the right and left sides of the figures. Large-angle grain boundaries are found in high density inside the clusters. Outside, the planar interface still exists, revealing defect bands formed by the first, semicoherent reaction mechanism. Overviews representing larger interface regions after different annealing times are reproduced in Fig. 13. The early interdiffusion stages of Cu/Au are by no means understood as a planar layer reaction. This becomes particularly clear by the extremely rough interfaces and surfaces induced by heterogeneous nucleation and transport during 20 s annealing.

Two important aspects of the identified recrystallization mechanism must be emphasized. (i) In HCDF images like those of Fig. 12, discontinuous composition profiles are noticed across the grain boundaries. This becomes particularly clear at the positions marked by arrows. Probably, most of the other boundaries are not aligned parallel to the optical axis, so that apparently continuous profiles result as an artifact of image projection. Therefore, we conclude that discontinuous composition steps at the grain boundaries are likely to represent the general case rather than the exceptional one.

(ii) The observed second reaction step is not sufficiently described as diffusion-induced grain boundary migration (DIGM). Instead, we observe nucleation of *new* grain orientations which is particularly obvious inside the Cu substrates, where the single crystal is split into many grains of different orientation. Thus, we observe a recrystallization process that decreases the grain size—as opposed to conventional recrystallization; here, an initially single-crystalline or coarse-grained microstructure is transformed into a nanocrystalline one.

VI. DISCUSSION

The presented experimental study yields clear evidence that the early interdiffusion of the lattice-mismatched metals Cu and Au proceeds by two subsequent reaction stages, as sketched in Fig. 14. In the first, semicoherent stage (a), the epitaxial orientation relationship is preserved. Relaxation of diffusion-induced strain and, in the case of the twin-type boundary, the required rotation of the lattice is achieved by climb and glide of dislocations. The second, incoherent reaction stage (b) is characterized by nucleation of new grains and migration of high-angle grain boundaries.

A. Semicoherent reaction stage

Several features of the planar diffusion zone established during the first reaction stage are quite remarkable. The measured composition profiles develop symmetrically between Cu and Au, and no Kirkendall voids are observed, although bulk diffusion data[7] predict a higher diffusion rate inside the Au layer with Cu being the more mobile species. This may indicate that the vacancy density is far from equilibrium in this early reaction stage, which is distinguished by high composition gradients and diffusion lengths much smaller than the typical distance between efficient vacancy sinks.

Furthermore, the profiles vary continuously across the composition range, which is only understood if most of the diffusion-induced stress relaxes by the observed structural

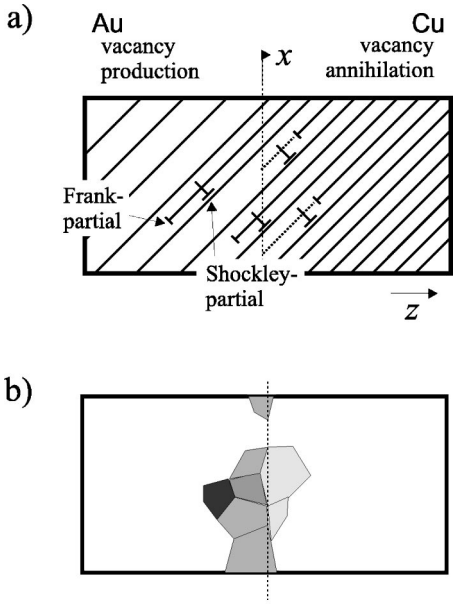

FIG. 14. Two stages of interdiffusion in Cu/Au: (a) semicoherent reaction by volume diffusion, (b) discontinuous reaction by recrystallization and grain boundary migration.

defects. This is clarified by the following quantitative consideration: Let us assume for the moment an Au layer that is rigidly attached to the Cu substrate, such that no relaxation occurs along the lateral directions (x and y axes). As a consequence, the chemically induced variation of the lattice parameter is counteracted by a dilatational stress[28]

$$\sigma_{xx}=\sigma_{yy}=\frac{E}{1-\nu}\,\eta c_{\mathrm{Cu}}, \tag{2}$$

which adds the elastic contribution

$$e=\frac{E}{1-\nu}\,\Omega\,\eta^2 c_{\mathrm{Cu}}^2 \tag{3}$$

to the system's free energy density. In these equations, E, ν, η, and Ω represent Young's modulus, Poisson's ratio, the misfit parameter $\eta=(a_{\mathrm{Cu}}-a_{\mathrm{Au}})/a_{\mathrm{Au}}$, and the atomic volume of Au, respectively. Thus, the interdiffusion potential $\partial f/\partial c$ must be modified by an elastic correction, which leads to the transport equation

$$j_z=-\frac{Dc_{\mathrm{Cu}}(1-c_{\mathrm{Cu}})}{kT}\left(\frac{\partial^2 f}{\partial c_{\mathrm{Cu}}^2}+\frac{2\Omega\,\eta^2 E}{1-\nu}\right)\frac{\partial c_{\mathrm{Cu}}}{\partial z} \tag{4}$$

$$=-D\left(1+\frac{c_{\mathrm{Cu}}(1-c_{\mathrm{Cu}})}{kT}\,\frac{2\Omega\,\eta^2 E}{1-\nu}\right)\frac{\partial c_{\mathrm{Cu}}}{\partial z}, \tag{5}$$

where the second term inside the brackets on the right-hand side accounts for the stress effect. The case of a Cu layer is formulated analogously; only the sign of the stress must be inverted and the material parameters adapted. Integrating Eq. (5) with appropriate elastic constants[29] $E_{\mathrm{Au}}=0.70\times10^{11}$ N/m^2, $\nu_{\mathrm{Au}}=0.428$, $E_{\mathrm{Cu}}=1.1\times10^{11}$ N/m^2, and $\nu_{\mathrm{Cu}}=0.356$, composition profiles are obtained as shown by the solid line (constrained) in Fig. 10. Because of the pronounced lattice mismatch, an elastically stabilized miscibility gap is predicted, extending from 20 to 80 at. % Cu. Similar discontinuities in the composition profile are also predicted in the more sophisticated analysis by Stephenson.[5] See, for example, the simulated profiles in recent work on interdiffusion of amorphous Ni/Zr.[6]

In contrast, in none of our experimental data do we observe any indication of such a compositional gap. Instead, the nanoanalysis always yields profiles in agreement with the conventional thick-film solution of Fick's laws, as indicated by the solid line (relaxed) in Fig. 10. Obviously, before reaching the elastic solubility limit of 20 at. % on either side of the profile, misfit dislocations move out of the interface, thereby reducing the stress efficiently. Based on the nanoanalytical data, we determine the critical composition for structural relaxation to about 10 at. % Cu and Au at the Au-rich and Cu-rich sides of the diffusion zone, respectively (see the boundaries of the defect band in Fig. 10). For this composition, a stress of 1.5 GPa is calculated with Eq. (2). This value exceeds the typical shear stress $\sigma_c=(10^{-4}-10^{-5})E$ of single-crystalline metals[30] already by two orders of magnitude, which indicates that stress levels required to induce the predicted miscibility gap are hardly achieved.

Most surprisingly, after a few seconds of annealing, the semicoherent reaction retards in a way that cannot be explained by ordinary parabolic growth. Either diffusion-induced stress or a nonequilibrium density of vacancies may be made responsible for this behavior. However, according to the presented estimates, the stress is probably not sufficient to explain such a drastic change of diffusion behavior like a complete stop of the reaction. Furthermore, neglecting relaxation, which would only decrease the elastic backstress, the expense of elastic energy scales proportional to the diffusion width, as does the gain of chemical energy, so that the existence of a limiting thickness cannot be understood by elastic effects.

Therefore, the observed retardation is very likely caused by a decrease of the vacancy density within the first few seconds of annealing. Further evidence for the important role of vacancies is seen in the different diffusion widths observed at the interface between the single-crystalline substrate and a deposited layer and that between two deposited layers, as presented in Fig. 10 of a previous publication.[11] Although not directly influenced by grain boundary diffusion, the latter diffusion zone is observed to be twice as thick as the former one, which is presumably due to an initial supersaturation of vacancies or their faster equilibration inside the deposited, polycrystalline layers.

To explain such a vacancy depletion we considered the annealing of nonequilibrium vacancies introduced during film deposition. However, it is doubtful whether the initial supersaturation could be sufficient to yield an apparent reaction stop. Therefore, it is suggested that in addition the semicoherent diffusion mechanism itself provides an effective sink, which annihilates vacancies inside the diffusion zone. This is justified by the following model calculation.

As revealed by HREM, climb of prismatic dislocations provides the dominant plastic relaxation mechanism. Dislo-

cations which climb towards the Au side generate vacancies; those climbing towards the Cu side annihilate them. If these two processes are not balanced, a total loss of vacancies may appear. For the sake of simplicity, we assume a simple cubic lattice with a microstructure similar to that sketched in Fig. 14(a), but the set of common lattice planes aligned normal to the interface. Consider the limiting case of complete relaxation in which the lattice mismatch along the x axis is immediately accommodated by climb of dislocations. In this case, we expect for the number M of planes stacked along the x axis

$$M(c_{\mathrm{Cu}}) = \frac{L}{a_{\mathrm{Au}}(1-\eta c_{\mathrm{Cu}})}, \tag{6}$$

if the lattice parameter of the alloy follows Vegard's law, a reasonable approximation to the behavior of disordered CuAu alloys.[31]

Remarkably, this relation is by no means linear with respect to the composition, which has an important consequence to the vacancy balance. Regarding the variation with local composition

$$\frac{\partial M}{\partial c_{\mathrm{Cu}}} = \frac{L\eta}{a_{\mathrm{Au}}(1-\eta c_{\mathrm{Cu}})^2}, \tag{7}$$

it is obvious that insertion and removal of lattice planes proceeds asymmetrically on the Au and Cu sides, respectively. A variation of M within a slab of thickness $\triangle z$ changes the number of vacancies by

$$dN_{\mathrm{Vac}} = \frac{L\triangle z}{a_{\mathrm{Au}}^2(1-\eta c_{\mathrm{Cu}})^2}\frac{\partial M}{\partial c_{\mathrm{Cu}}}dc_{\mathrm{Cu}}, \tag{8}$$

causing a change of the local vacancy fraction:

$$dc_{\mathrm{Vac}} = dN_{\mathrm{Vac}}\frac{a_{\mathrm{Au}}^3(1-\eta c_{\mathrm{Cu}})^3}{L^2\triangle z} \tag{9}$$

$$= \frac{a_{\mathrm{Au}}(1-\eta c_{\mathrm{Cu}})}{L}\frac{\partial M}{\partial c_{\mathrm{Cu}}}dc_{\mathrm{Cu}} \tag{10}$$

$$= \frac{\eta}{1-\eta c_{\mathrm{Cu}}}dc_{\mathrm{Cu}}. \tag{11}$$

If the composition profile develops symmetrically in the sense that $dc/dt|_c = -dc/dt|_{1-c}$, more vacancies are annihilated on the Cu side than produced on the Au side. To determine the behavior also in the case of asymmetric atomic mobilities, we have to solve the diffusion problem inside a bilayer specimen of double-layer thickness w. The outer boundaries are assumed to be impermeable, which corresponds to a multilayer, where the flux of all species vanish in the middle of the layers, as required by the specimen's symmetry. Independent site exchanges of Cu-Vac and Au-Vac pairs are considered, which results in the ansatz for the particle flux,

$$\begin{pmatrix} j_{\mathrm{Cu}} \\ j_{\mathrm{Vac}} \\ j_{\mathrm{Au}} \end{pmatrix} = \begin{pmatrix} -D'_{\mathrm{Cu}}c_{\mathrm{Vac}} & D'_{\mathrm{Cu}}c_{\mathrm{Cu}} & 0 \\ D'_{\mathrm{Cu}}c_{\mathrm{Vac}} & -D'_{\mathrm{Cu}}c_{\mathrm{Cu}} - D'_{\mathrm{Au}}c_{\mathrm{Au}} & D'_{\mathrm{Au}}c_{\mathrm{Vac}} \\ 0 & D'_{\mathrm{Au}}c_{\mathrm{Au}} & -D'_{\mathrm{Au}}c_{\mathrm{Vac}} \end{pmatrix} \times \frac{\partial}{\partial z}\begin{pmatrix} C_{\mathrm{Cu}} \\ C_{\mathrm{Vac}} \\ C_{\mathrm{Au}} \end{pmatrix}, \tag{12}$$

and the evolution of the atomic densities

$$\frac{dC_{\mathrm{Cu}}}{dt} = -\frac{\partial}{\partial z}j_{\mathrm{Cu}} \tag{13}$$

$$\frac{dC_{\mathrm{Au}}}{dt} = -\frac{\partial}{\partial z}j_{\mathrm{Au}} \tag{14}$$

$$\frac{dC_{\mathrm{Vac}}}{dt} = -\frac{\partial}{\partial z}j_{\mathrm{Vac}} + \frac{\eta}{1-\eta c_{\mathrm{Cu}}}\left(c_{\mathrm{Cu}}\frac{\partial}{\partial z}j_{\mathrm{Au}} - c_{\mathrm{Au}}\frac{\partial}{\partial z}j_{\mathrm{Cu}}\right). \tag{15}$$

In these equations, capital letters C_i denote concentrations per volume, whereas small letters c_i denote atomic fractions. The second term on the right-hand side of Eq. (15), accounting for vacancy production and annihilation, was derived from Eq. (11) obeying $c_{\mathrm{Cu}} \approx C_{\mathrm{Cu}}/(C_{\mathrm{Cu}}+C_{\mathrm{Au}})$. The diffusivities $D'_{\mathrm{Cu}} = D_{\mathrm{Cu}}/c_{\mathrm{Vac}}^{(\mathrm{eq})}$ and $D'_{\mathrm{Au}} = D_{\mathrm{Au}}/c_{\mathrm{Vac}}^{(\mathrm{eq})}$ may vary with composition, depending on the system under consideration. In order to limit the computing time, the initial vacancy fraction is chosen to $c_0 = 10^{-5}$, which is artificially high compared to the experimental value.

In Fig. 15, two examples of model calculations are presented. For the example (a), $D_{\mathrm{Cu}} = D_{\mathrm{Au}} = D = \mathrm{const}$ is assumed. At the very beginning of the reaction (atomic diffusion length $10^{-4}w$), a vacancy supersaturation is still evolving on the Au side, but subsequently the annihilation of vacancies on the Cu side dominates the reaction, and an overall vacancy depletion results. In calculation (b), $D_{\mathrm{Cu}} = D(1+100c_{\mathrm{Au}})$ and $D_{\mathrm{Au}} = D(1+10c_{\mathrm{Au}})$ is assumed, which resembles the behavior of AuCu expected from bulk diffusion data; compared to pure Cu, the bulk diffusion in pure Au is much faster, and, furthermore, Cu atoms are more mobile than Au atoms.[7] In this case, at first a vacancy supersaturation develops at the Cu side because of the difference in the atomic mobilities. However, similar to the former example, the reaction zone is depleted of vacancies in later stages. Similar calculations were performed for several other choices of the relative diffusivities. In all cases the vacancy density is finally controlled by the predominant annihilation on the Cu side.

Certainly, the real situation is more complex than assumed in our simplified model. Vacancy densities deviating from equilibrium themselves will produce an osmotic climb force to dislocations,[32] which counteracts the elastic climb force. Eventually, the prismatic dislocations follow the interdiffusion with a certain delay, so that our assumption of instantaneous and complete stress relaxation is only a crude first

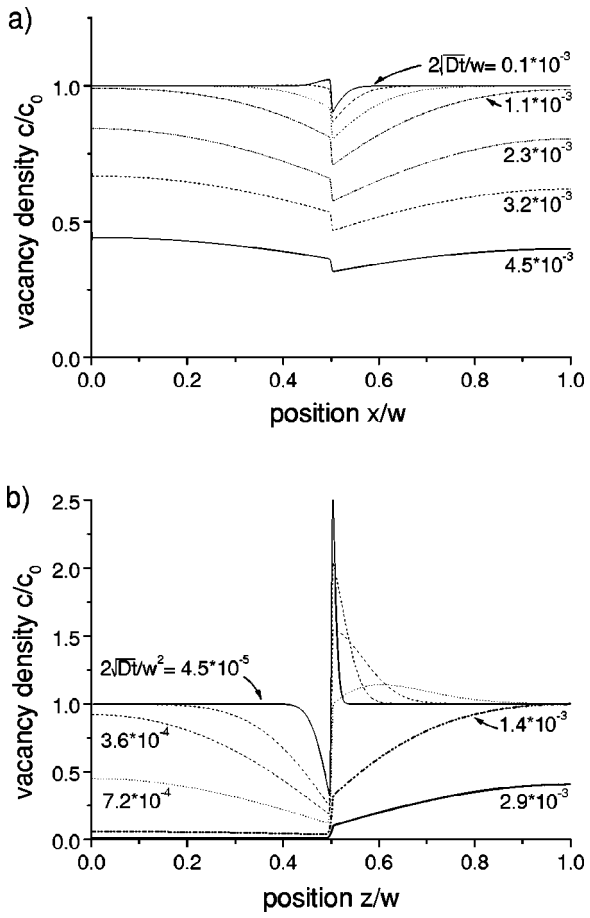

FIG. 15. Model calculation of vacancy density during the semicoherent reaction stage. The reaction time is characterized by the diffusion length of the atomic transport. w denotes the thickness of the sample; the interface is located at $z=w/2$. The initial vacancy fraction c_0 was chosen to 10^{-5}. (a) Equal mobility of the species in both phases, (b) faster diffusion inside the Au layer, with Cu being the more mobile element.

approximation. In addition, other neutral vacancy sinks or sources, like glissile edge dislocations or grain boundaries, are neglected, and the initial vacancy density is overestimated. But despite these limitations, at least the existence of a significant driving force for vacancy annihilation, induced by the coherency constraint, can be inferred. In this way, the calculations support the hypothesis that the reaction stop is caused by vacancy depletion. In consequence, the reaction is not directly affected by the induced stress but indirectly by the stress-induced nonequilibrium of point defects.

B. Incoherent reaction stage

As the coherent reaction slows down after very short annealing, an effective reduction of the system's free energy is only possible by a second mechanism. New grains are nucleated at the interface, introducing high-angle grain boundaries, which allow to restore the vacancy equilibrium and to relax induced stress. As concluded from HCDF images, the previously continuous diffusion zone splits into homogeneous regions of different composition. This interpretation is

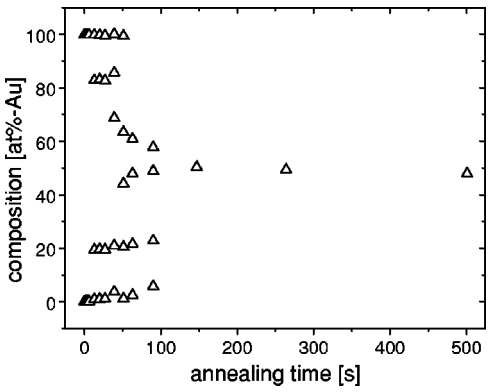

FIG. 16. Dominant compositions inside the reaction zone as derived from the peak intensities of the x-ray spectra in Fig. 8.

further supported by the x-ray diffractograms presented in Fig. 8. Using Vegard's law to interpret the position of the intensity maxima, the preferred compositions of newly formed grains are inferred as shown in Fig. 16. At about 10 s annealing, a first generation of grains nucleates at both sides of the interface, having a composition difference of about 20 at. % to the surrounding pure Cu and Au. After further annealing for 30 s, a second generation of grains forms, showing roughly the same composition difference to their surrounding, comprised of grains of the first generation. Later, the grains of the first generation disappear while those of the second generation continuously equalize their composition to merge finally to the average composition of the specimen. It should be pointed out that the number and the absolute values of the observed compositions 20, 43, 69, and 82 at. % Au are incompatible with the ordered compounds known in the system at lower temperatures. This reveals that the described behavior is controlled by kinetic rather than thermodynamic factors.

Regarding the considerable chemical driving force provided by the chemically abrupt interface, a nucleation process with a clear incubation period and heterogeneous nucleation sites is surprising. By calorimetry, the mixing enthalpy of equal amounts of Cu and Au is determined to 5.3 kJ/mol. Hence, assuming a regular solution, the chemical driving force to form the observed grains with a composition of 20 at. % is estimated to $f_v=7.4\times10^{-5}$ kJ/m^3. If a specific interface energy of $\gamma=600$ mJ/m^2 is assumed, a typical value of large-angle grain boundaries in Cu, the diameter of a nucleus is predicted to

$$d=\frac{4\sigma}{f_v}=3 \text{ nm}. \tag{16}$$

This value is indeed too small to explain the observed heterogeneous nucleation and the average grain size of the observed grains in the recrystallized regions. However, by analogy to DIGM, where the question of the appropriate driving force was already addressed by careful experiments,[33] it is suggested that not the total gain of chemical energy, but only the contribution of the strain field and structural defects may be considered to drive the microstructural transformation.

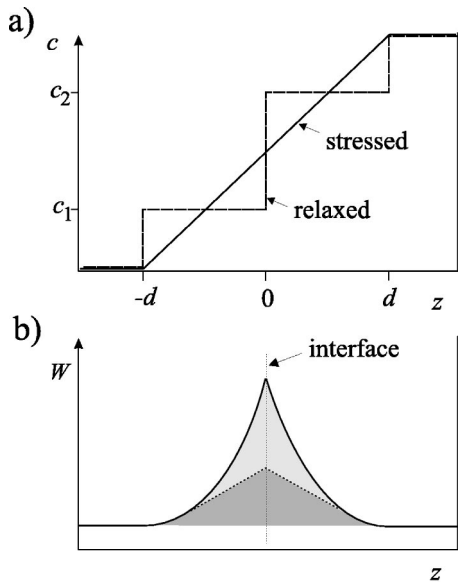

FIG. 17. Schematic composition profile through the diffusion zone (a) and stored energy of the stressed case (b).

In this case, the size of a nucleus may be estimated by comparing (i) a stressed rectangular volume $d\times d\times 2d$ containing a continuous composition variation of diffusion length $2d$ with (ii) two relaxed grains at both sides of the interface with a different but homogeneous composition; see the schematic composition profiles in Fig. 17(a). To avoid complex geometric factors, we assume a linear composition profile and cubic grains of edge size d. The elastic energy in case (i) is determined by

$$E_{\text{elast}}=2d^2\frac{E}{1-\nu}\eta^2\int_0^d \triangle c(z)^2 dz \tag{17}$$

$$=2d^2\frac{E}{1-\nu}\eta^2\int_0^d \frac{1}{4}\left(1-\frac{z}{d}\right)^2 dz \tag{18}$$

$$=\frac{d^3}{6}\frac{E}{1-\nu}\eta^2, \tag{19}$$

where we made use of Eq. (3). This has to be compared to the energy of the grain boundaries in case (ii):

$$E_{\text{GB}}=12d^2\gamma. \tag{20}$$

Thus, the nucleus size is determined by

$$\frac{\partial}{\partial d}\left(12d^2\gamma-\frac{1}{6}\frac{E}{1-\nu}\eta^2 d^3\right)=0, \tag{21}$$

which yields

$$d=48\frac{\gamma(1-\nu)}{E\,\eta^2}. \tag{22}$$

Inserting average material constants $\gamma=0.6$ J/m^2, $E=0.9\times10^{11}$ N/m^2, and $\nu=0.39$, the size of a critical grain is predicted to ≈ 15 nm. In this calculation, plastic relaxation has been neglected. Relaxation would reduce the quadradic composition dependence of the stored energy to a linear one, as soon as $\triangle c$ exceeds the observed elastic limit of about 10 at. %; see the dotted line in Fig. 17(b). Thus, as indicated by the area below the energy curve in the figure, the total driving force might be decreased to one-half. Consequently, a nucleus size of a few tens of nm is quite realistic and in agreement to the early grains observed in the micrographs (see, e.g., Fig. 9). Furthermore, it makes clear that the onset of the second reaction step is only possible after an incubation period of 10 s, during which the necessary driving force is built up by interdiffusion throughout a depth of 15–20 nm.

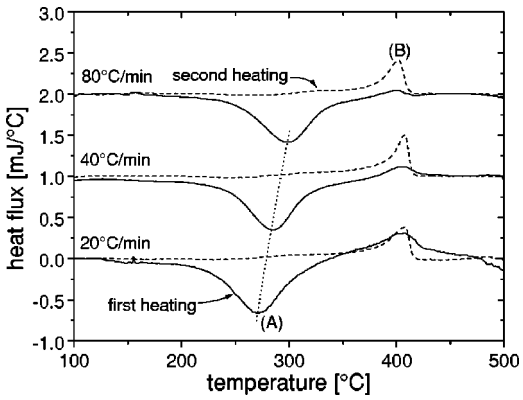

FIG. 18. DSC measurement of the reaction of a Au/Cu multilayer (50-nm single-layer width). First heating is shown by solid lines, second heating by dashed lines. The shift of the exothermic peak (a) with heating rate is emphasized by a dotted line.

By the nucleation of grains, mobile high-angle grain boundaries are introduced into the formerly epitaxial configuration. This is reflected by very fast reaction rates and low activation energies seen by calorimetry. In Fig. 18, thermograms of the reaction are presented, obtained with several different heating rates. During the first heating of freshly prepared specimens, the interdiffusion gives rise to the exothermic heat marked by (A). The endothermic peak (B), which becomes particularly clear during a second heating of the already mixed samples, is due to disordering above the order transition temperature. The mixing peak (A) shifts towards higher temperatures with increasing heating rate, which allows one to determine the activation energy of the reaction using the method of Kissinger.[34] A value of $E_{\text{act}}=1.18$ eV is found,[13] which is significantly smaller than the ≈ 2 eV determined for volume diffusion in massive Cu or Au,[35,36] but closer to the 0.87 and 1.09 eV measured for grain boundary diffusion in both metals.[37,38]

Obviously, beside the relaxation of stress and vacancy density, the grain boundaries provide transport paths along which Cu and Au can intermix quickly. A complete transformation of the volume is achieved by the migration of these boundaries (DIGM), so that the boundary mobility becomes the dominating factor to control the kinetics. Regarding this boundary migration mechanism, the second interdiffusion stage develops quite similarly to the intermixing observed in nanocrystalline Pb/AgPd layers (Ref. 39) and Ag/Pd layers (Refs. 40 and 41), where grain boundaries existed from the beginning. However, in our epitaxial specimens the reaction

requires an additional important step, which consists of producing the necessary transport paths to accelerate the kinetics. This has an important consequence to the design of diffusion barriers, where it is an accepted rule to avoid grain boundaries. In the case of lattice-mismatched systems this may not be sufficient.

It is remarkable that already in 1983 den Broeder *et al.*[42] compared the interdiffusion in the reactive systems Cu/Al and Au/Al, where the respective lattice mismatch is quite similar to that of the Cu/Au and Ag/Au studied here. They noticed migration of grain boundaries only in Cu/Al, but could not work out a clear reason for the difference between both systems. From the present study, it is suggested that the lattice mismatch between the reacting materials is the important factor.

It was already pointed out that the preferred compositions observed in the reaction zone are not stabilized thermodynamically but result from kinetics. It seems clear that the composition inside the newly formed grains is determined by the balance between the grain boundary migration velocity and the transport of atoms through the grain boundary.[43] However, it is striking that the composition difference between the pure materials and grains of first generation on the one hand and that between grains of first and second generations on the other hand are almost identical, although in the latter case the grain boundary diffusion should be already significantly slowed down since part of the driving force is already released. The close correspondence between the composition difference and the elastic solubility limit of about 20 at. % predicted by Eq. (5) suggests that these two phenomena are somehow related, but no clear relation could be worked out yet.

C. Consequences to the formation of ordered compounds

Besides the DSC measurements, all data presented so far refer to the interdiffusion of Cu and Au at temperatures that exclude the formation of ordered compounds. However, the two-stage reaction mechanism identified here is also effective at lower temperatures, where the ordered compounds Cu_3Au, CuAu, and $CuAu_3$ may form. Studying the isothermal reactions at 230°C and 350°C by TEM and XRD, we observe a similar microstructural development, characterized by the initial planar defect zone and the ''inverse'' recrystallization mechanism.[13] Remarkably, the maximum width of the defect zone developed at 230°C amounts to 15 nm, almost identical to the width determined at 430°C, which confirms the existence of a maximum diffusion length in the first reaction step. Only the time scale must be adjusted to the reduced atomic mobility. The incubation period of the second reaction step is determined to >1 min and >220 min at 350°C and 230°C, respectively. Thus, the influence of the phase formation on the mixing kinetics seems to be negligible.

This behavior can be elucidated by the thermograms in Fig. 18. The exothermic peak A is related to mixing and the endothermic peak B to disordering. Comparing the peak areas, it is quite obvious that the ordering enthalpy amounts to at most one-third of the mixing enthalpy, $\triangle H_{\mathrm{mix}} = 40.4$ J/g and $\triangle H_{\mathrm{order}} = 13.6$ J/g (see also data by Sundman *et al.*[44]). Thus, the dominating driving force to the reaction is due to mixing, while the lattice order provides only a minor contribution. Furthermore, comparing the mixing and disordering peaks of first heating with 80°C/min, it is seen that at the end of the heating run intermixing is almost completed, whereas ordering is significantly suppressed. Obviously, instead of being concomitant, mixing and ordering are subsequent processes, where the major gain of free energy is already achieved by the first mixing reaction. Thus, it is not surprising that a very similar structural transformation is observed above and below the ordering transition temperature.

Tu and Berry[45] studied the interreaction of Cu/Au thin films by x-ray diffractometry and Borders[46] by Rutherford backscattering. Both experimental techniques do not provide lateral information on the required scale of 10–100 nm. Furthermore, the existence of ordered reaction products was not explicitly proved e.g., by superlattice reflections, but only concluded from the composition of the reaction zone. Owing to insufficient lateral information, both studies could only assume the formation of planar product layers. Our microscopic investigation, however, demonstrates that this assumption is not valid. As the RBS analysis of Borders averaged laterally on regions of different reaction progress, he observed a continuous transition instead of different plateaus in composition profiles normal to the interface. From reflection intensities in their x-ray spectra Tu and Berry derived a reaction kinetics linear in time, which they claim to be caused by a kinetic barrier at the interface between ordered and disordered phases. Beside the limitation that their data analysis relies on a persistent layer geometry, our results demonstrate that the overwhelming part of the intermixing reaction proceeds without ordering. Thus, deviation from parabolic growth must be explained by the required nucleation, grain boundary transport and migration, and the very complicated morphology of the reaction zone. As these factors are effective above the order transition temperature as well as below, no dramatic change in the mixing kinetics is seen between these two temperature regimes, in contradiction to the assumption of Tu and Berry.

VII. CONCLUSIONS

The atomistic mechanisms of interdiffusion in metallic thin films have been investigated by microscopic structural and chemical analysis. Comparing the results of lattice-matched Au/Ag and lattice-mismatched Au/Cu, the study has focused on the influence and relaxation of reaction induced misfit. In the case of Cu and Au, distinguished by a large lattice mismatch of 12%, the early interdiffusion stages develop in a more complex fashion than expected from Fick's laws.

(i) In spite of the considerable mismatch, epitaxial growth is observed in sputter-deposited Cu and Au layers. Two preferred orientation relations dominate, corresponding to a $\Sigma = 1$ and $\Sigma = 3$ orientation relationship for homophase boundaries.

(ii) At these two interface types, interdiffusion proceeds in two subsequent steps. During the first, semicoherent reaction

stage, the relaxation of mismatch stress and the required lattice rotation is achieved by climb and glide of dislocations. The reaction stops after reaching a temperature-independent diffusion length of about 17 nm. It is suggested that this stop is due to a vacancy depletion caused by dislocation climb inside the reaction zone. The onset of the second, incoherent stage is found after a temperature-dependent incubation period.

(iii) During the second reaction stage, recrystallization of the reaction zone takes place. Instead of continuous diffusion profiles, discontinuous composition steps at the boundaries and preferred compositions inside the grains are observed. The atomic transport proceeds by grain boundary diffusion and migration. Because of heterogeneous nucleation and transport, the initial planar geometry is destroyed. The size of the nucleated grains and the necessary incubation time can be modeled by considering simply the elastic contribution to the free energy as the driving force for microstructural transformations.

(iv) Owing to the low ordering enthalpies of the compounds in AuCu, the interdiffusion is hardly influenced by the formation of ordered compounds. Above and below the critical temperatures for ordering, identical microstructural mechanisms are identified.

ACKNOWLEDGMENTS

Financial support by the Deutsche Forschungsgemeinschaft (SCHM 1182/1-2) is gratefully acknowledged.

*Corresponding author. Electronic address: guido@umpa03.gwdg.de

[1] J.W. Cahn and J.E. Hilliard, J. Chem. Phys. **28**, 1085 (1958).
[2] H.E. Cook and J.E. Hilliard, J. Appl. Phys. **40**, 2191 (1969).
[3] F.C. Larché and J.W. Cahn, Acta Metall. **30**, 1835 (1982).
[4] F.C. Larché and J.W. Cahn, Acta Metall. **33**, 331 (1985).
[5] G.B. Stephenson, Acta Metall. **36**, 2663 (1988).
[6] A.L. Greer, Defect Diffus. Forum **129-130**, 163 (1996).
[7] H. Mehrer, in *Diffusion in Solid Metals and Alloys*, edited by D. Madelung, Landoldt Börnstein, New Series, Group III, Vol. 26, pt. 81 (Springer, Verlag, Berlin, 1990).
[8] Victawet delivered by PLANO.
[9] A. Romano, J. Vanhellemont, H. Bender, and J.R. Morante, Ultramicroscopy **31**, 183 (1989).
[10] M.M.J. Treacy and J.M. Gibson, Ultramicroscopy **52**, 31 (1993).
[11] G. Schmitz, J. Ewert, and F. Hartung, Ultramicroscopy **77**, 49 (1999).
[12] P. Haasen, *Physical Metallurgy* (Cambridge University Press, Cambridge, England, 1996), p. 123.
[13] F. Hartung, Ph.D. thesis, University of Göttingen, 2000.
[14] J.E. Marcur and R.W. Vook, Thin Solid Films **66**, 371 (1980).
[15] J.H. van der Merwe, J. Appl. Phys. **34**, 123 (1963).
[16] P. Pirouz, F. Ernst, and Y. Ikuhara, Solid State Phenom. **59-60**, 51 (1998).
[17] G. Gladyszewski, Thin Solid Films **204**, 473 (1991).
[18] T. Jeske and G. Schmitz, Mater. Sci. Eng. (to be published).
[19] J. Schleiwies and G. Schmitz, Mater. Sci. Eng. (to be published).
[20] C. Lang, G. Schmitz, and R. Kirchheim Defect Diffus. Forum **194-199**, 1525 (2001).
[21] W.A. Johnson, Trans. AIME **147**, 331 (1942).
[22] H.E. Cook and J.E. Hilliard, J. Appl. Phys. **40**, 2191 (1969).
[23] K. Meinel, M. Klaua, and H. Bethge, Thin Solid Films **34**, 157 (1976).
[24] S.K. Wonnel, J.M. Delaye, M. Bibole, and Y. Limoge, J. Appl. Phys. **72**, 5195 (1992).
[25] F.-L. Yang, A.L. Greer, and R.E. Somekh, Thin Solid Films **275**, 258 (1996).
[26] J.C. Ewert, F. Hartung, and G. Schmitz, Appl. Phys. Lett. **71**, 1311 (1997).
[27] P.A. Stadelmann, Ultramicroscopy **21**, 131 (1987).
[28] W.D. Nix, Metall. Trans. A **20**, 2217 (1989).
[29] G. Simmons and H. Wang, *Single Crystal Elastic Constants and Calculated Aggregate Properties* (Cambridge University Press, Cambridge, England, 1971).
[30] J. Weertman and J. R. Weertman, in *Physical Metallurgy*, edited by R. Cahn and P. Haasen (North-Holland, Amsterdam, 1983), p. 1305.
[31] W. B. Pearson, *A Handbook of Lattice Spacing and Structures of Metals and Alloys* (Pergamon Press, London, 1967), Vol. II.
[32] J. P. Hirth and J. Lothe, *Theory of Dislocations* (McGraw-Hill, New York, 1982).
[33] D.N. Yoon, Annu. Rev. Mater. Sci. **19**, 43 (1989).
[34] H.E. Kissinger, Anal. Chem. **29**, 1702 (1957).
[35] S. Fujikawa, M. Werner, H. Mehrer, and A. Seeger, Mater. Sci. Forum **15-18**, 431 (1987).
[36] C.T. Tomizuka, Bull. Am. Phys. Soc. **2**, 123 (1957).
[37] A.E. Austin, N.A. Richard, and E. Wood, J. Appl. Phys. **37**, 3651 (1966).
[38] A. Chatterjee and D.J. Fabian, Acta Metall. **17**, 1141 (1969).
[39] K.N. Tu, J. Appl. Phys. **48**, 3400 (1977).
[40] V.M. Kosevich, A.N. Gladkikh, M.V. Karpowsky, and V.N. Klimenko, Int. J. Neural Syst. **2**, 247 (1994); **2**, 261 (1994); **2**, 271 (1994);
[41] V.M. Kosevich, V.N. Klimenko, A.N. Gladkikh, and M.V. Karpowsky, Int. J. Neural Syst. **3**, 151 (1995).
[42] F.J.A. den Broeder, M. Klerk, J.M. Vandenberg, and R.A. Hamm, Acta Metall. **31**, 285 (1983).
[43] J.W. Cahn, J.D. Pan, and R.W. Balluffi, Scr. Metall. **13**, 503 (1979).
[44] B. Sundmann, S.G. Fries, and W.A. Oates, Z. Metallkd. **90**, 4 (1999).
[45] K.N. Tu and B.S. Berry, J. Appl. Phys. **43**, 3283 (1972).
[46] J.A. Borders, Thin Solid Films **19**, 359 (1973).